

## SUPPLEMENTARY INFORMATION

### **Dual-phase modulation via Mo doping and Li<sub>3</sub>PO<sub>4</sub> coating for stabilized LiNi<sub>0.9</sub>Mn<sub>0.07</sub>Co<sub>0.03</sub>Al<sub>0.01</sub>O<sub>2</sub> cathodes in high-energy lithium-ion batteries**

Srinivasan Alagar<sup>a</sup>, Jun Kim<sup>a</sup>, Eun-Jung Shin<sup>b</sup>, Alex Ditter<sup>c</sup>, David A. Shapiro<sup>c</sup>, Namdong Kim<sup>d</sup>, Won Gi Hong<sup>e,h</sup>, Hyungsub Kim<sup>\*.f,h</sup>, Young-Sang Yu<sup>\*.b,h</sup>, Gi Dae Park<sup>\*.g,h</sup> Sang Mun Jeong<sup>\*.a,h</sup>

<sup>a</sup>*Department of Chemical Engineering, Chungbuk National University, Cheongju, Chungbuk 28644, Republic of Korea, E-mail: smjeong@chungbuk.ac.kr*

<sup>b</sup>*Department of Physics, Chungbuk National University, 1 Chungdae-ro, Seowon-gu, Cheongju-si, Chungbuk-do 28644, Republic of Korea*

<sup>c</sup>*Advanced Light Source, Lawrence Berkeley National Laboratory, Berkeley, CA 94720, USA*

<sup>d</sup>*Pohang Accelerator Laboratory, Pohang University of Science and Technology, Pohang 37673, Republic of Korea*

<sup>e</sup>*Research Center for Materials Analysis, Korea Basic Science Institute, Daejeon, Republic of Korea, E-mail: hyungsubkim@kaeri.re.kr*

<sup>f</sup>*Neutron Science Division, Korea Atomic Energy Research Institute (KAERI), 111 Daedeok-daero 989, Beon-Gil, Yuseong-gu, Daejeon 34057, Republic of Korea, E-mail: youngsang@chungbuk.ac.kr*

<sup>g</sup>*Department of Advanced Materials Engineering, Chungbuk National University, Chungdae-ro 1, Seowon-Gu, Cheongju, Chungbuk 28644, Republic of Korea, E-mail: gdpark@chungbuk.ac.kr*

<sup>h</sup>*Advanced Energy Research Institute, Chungbuk National University, Chungdae-ro 1, Seowon-gu, Cheongju 28644, Republic of Korea*

## Materials characterization

The crystal structures of NMCA, Mo-NMCA, and LPO-coated Mo-NMCA were characterized using X-ray diffraction (XRD) and neutron diffraction (ND) analyses. XRD data were collected by D8 Discover with GADDS, Bruker. ND data were obtained with a high-resolution powder diffractometer (HRPD) at the High-Flux Advanced Neutron Application Reactor (HANARO) facility of the Korea Atomic Energy Research Institute (KAERI). Measurements were conducted over the  $2\theta$  range of  $0^\circ$ – $160^\circ$  with a step size of  $0.05^\circ$  and a constant wavelength of  $1.834478 \text{ \AA}$ . Field emission scanning electron microscopy (FE-SEM, Carl Zeiss, LEO-1530). High-resolution TEM was conducted using a JEOL JEM-2100F operating at 200 kV, with imaging performed under low-dose conditions to minimize beam-induced artifacts. To enhance lattice visibility while preserving structural fidelity, only mild FFT-based noise filtering and linear brightness adjustments were applied using Gatan DigitalMicrograph. Lattice analysis was restricted to well-aligned, drift-free regions located near the thin particle edges, selected for their superior electron transparency. X-ray photoelectron spectroscopy (XPS, PHI Quantera II) was employed to detect information regarding the surface chemical compositions.

To further substantiate the synergistic influence of Mo doping and LPO coating on either bulk or surface-localized regions of NCMA, two-dimensional image spectra (i.e., repeated images at different energies) across the Ni *L*-absorption edge were acquired for both as-prepared NCMA and LPO-Mo-NCMA using scanning transmission X-ray microscopy (STXM) and high-resolution ptychography. These measurements were performed at the Advanced Light Source (ALS), Lawrence Berkeley National Laboratory (Berkeley, California, USA), on the elliptically polarizing undulator beamline (7.0.1.2 COSMIC, coherent X-ray scattering and microscopy) <sup>1</sup>. The averaged XAS spectra for the cycled LPO-Mo-NCMA sample were measured using the 10A1 STXM at the

Pohang Light Source-II (PLS-II), Pohang Accelerator Laboratory (Pohang, Republic of Korea) <sup>2</sup>. The cycled LPO-Mo-NCMA sample was harvested after 200 repeated charge/discharge cycles within a voltage window of 2.8–4.3 V at an 3 C rate and 25 °C. For both beamlines, a coherent-monochromatic X-ray beam focused onto the sample by a Fresnel zone plate with an outer-zone width of 45 or 60 nm and an order-sorting aperture. Two-dimensional raster scans of the transmitted and scattered X-rays were acquired via either an X-ray sensitive PIN diode point-detector (for STXM) or a two-dimensional fast charge-coupled device (CCD, for ptychography). To accelerate the measurement speed, a specially designed spiral scan route driven by arbitrary controllable motions in  $x$ - and  $y$ -piezo motors, was adopted for STXM measurements at the ALS <sup>3</sup>.

Considering the penetration depths of the samples near the Ni  $L$ -edge, all harvested secondary particles, either from pristine powder or cycled cathodes, were pre-treated using a focused-ion-beam (FIB) instrument (Helios G4, FEI or NX5000, Hitachi) to produce approximately 150-nm-thick sections, which were then attached to Mo lift-out grids (Omniprobe #460-223, Ted Pella, INC.). For the selected sample regions, image spectra across the Ni  $L$ -edge were recorded with the finest 0.25 eV step near the absorption resonance, pixel sizes ranging from 25 to 50 nm, and dwell times from 0.25 to 2 ms. The scan parameters were primarily determined by the time consumption associated with the sample size and required image quality. The transmitted X-ray intensities at each raster point in STXM measurements were directly converted into optical density (OD) using Beer's law. In contrast, high-resolution ptychography required an additional step to reconstruct the real-space image from a series of diffraction patterns collected at raster points with larger step size (40 or 60 nm for focus or defocus modes) and proper overlaps. Details of the image reconstruction process adopted at the ALS 7.0.1.2 beamline can be found in the literature <sup>1</sup>. The diffraction data

processing, including ptychographic reconstruction and background retrieval <sup>4</sup>, was carried out using standard methods available in the SHARP-CAMERA software package with parallel computation (<http://camera.lbl.gov>). The converted OD images from both STXM and ptychography were aligned with sub-pixel accuracy using an iterative registration algorithm <sup>5</sup>. Pixel-by-pixel XAS spectra were extracted from the sample regions, defined by a global threshold of the mean OD image using Otsu's method <sup>6</sup>, while excluding low-signal-to-noise pixels based on the *R*-factor threshold higher than 0.10. The Ni oxidation state maps were quantitatively simulated using linear superpositions of the reference spectra for Ni<sup>2+</sup> (from LiMn<sub>1.5</sub>Ni<sub>0.5</sub>O<sub>4</sub> spinel) and Ni<sup>3+</sup> (from LiNi<sub>0.8</sub>Co<sub>0.15</sub>Al<sub>0.05</sub>O<sub>2</sub>), as shown in Fig. S12.

## Electrochemical Measurements

A cathode slurry was synthesized by blending the prepared cathode material (80 wt%), SuperP conductive carbon (10 wt%), and polyvinylidene fluoride (PVDF, 10 wt%) in N-methyl-2-pyrrolidone (NMP). The resulting mixture was uniformly coated onto 8 μm thick aluminum foil and subsequently dried, yielding electrodes with active material mass loadings ranging from 2 to 4 mg cm<sup>-2</sup>. The electrolyte was composed of a 1.0 M LiPF<sub>6</sub> solution in a 1:1 volumetric ratio of dimethyl carbonate (DMC) and ethylene carbonate (EC). For electrochemical performance evaluation, the synthesized cathode was assembled with a lithium metal counter electrode into a 2032-coin cell, employing a polypropylene separator (Celgard 2400) in an argon-filled glovebox. The electrochemical performance of the coin cells was characterized using a battery testing system, operating within a voltage window of 2.8–4.3 V at 25 °C. The charge and discharge rate of 1C, corresponding to 200 mAh g<sup>-1</sup>, was defined based on the theoretical capacity of NMCA. Electrochemical impedance spectroscopy (EIS) measurements were carried out using an Autolab

electrochemical workstation, spanning frequencies from 100 kHz to 0.001 Hz. Furthermore, the galvanostatic intermittent titration technique (GITT) was utilized to determine the lithium-ion diffusion coefficients during both charge and discharge processes <sup>7</sup>.

$$D_{Li^+} = \frac{4}{\pi\tau} \left( \frac{m_B V_M}{M_B S} \right)^2 \left( \frac{\Delta E_s}{\Delta E_\tau} \right)^2 \quad (1)$$

The diffusion coefficient of lithium ions ( $DLi^+$ ) was calculated using Fick's second law of diffusion, as shown in Equation (1), where  $m_B$  represents the mass of the active material (g),  $V_M$  is the molar volume ( $cm^3 mol^{-1}$ ),  $S$  is the electrode surface area ( $cm^2$ ), and  $M_B$  is the molecular weight of the active material ( $g mol^{-1}$ ). The cathode was employed as the working electrode, while both counter and reference electrodes were composed of lithium metal. The cyclic voltammetry was conducted at a scan rate of  $0.01 mV s^{-1}$ , with the voltage range set between 2.6 and 4.6 V. The charge/discharge and GITT characteristics of the cathode electrodes were measured at various scan rates on a Land system (WonATech, WBCS 3000). Electrochemical impedance spectroscopy (EIS, f: 100 kHz to 0.01 Hz, signal amplitude: 5 mV) and full cell pouch cell device performances were studied by using an Auto-lab electrochemical workstation (PGSTAT302N, Netherlands).

**XRD and FE-SEM of  $Ni_{0.90}Mn_{0.07}Co_{0.02}Al_{0.01}(OH)_2$ :** The X-ray diffraction (XRD) analysis (Fig. S1) reveals sharp and distinct peaks that correspond exclusively to the hexagonal  $Ni(OH)_2$  phase (JCPDS No. 74-2075), with no detectable signatures of  $Co(OH)_2$ ,  $Mn(OH)_2$  and  $Al(OH)_2$  phases. This observation confirms the successful formation of a solid-solution  $Ni_{0.90}Mn_{0.07}Co_{0.02}Al_{0.01}(OH)_2$  structure, with Mn, Co and Al atoms effectively integrated into the  $Ni(OH)_2$  lattice. Morphological analysis reveals that the  $Ni_{0.90}Mn_{0.07}Co_{0.02}Al_{0.01}(OH)_2$  precursor adopts a nearly spherical morphology, exhibiting an average particle size of approximately  $2.3 \mu m$

(Fig. S2a–d). High-magnification imaging (Fig. S2d) further uncovers that these micron-sized secondary particles are composed of densely packed, radially aligned primary nanoscale subunits. Elemental mapping obtained through energy-dispersive spectroscopy (EDS) (Fig. S2e) reveals a homogenous spatial distribution of Ni, Mn, Co, and Al. The analysis further verifies the precise molar ratios of these elements (Fig. S2f), aligning with the expected stoichiometric composition.

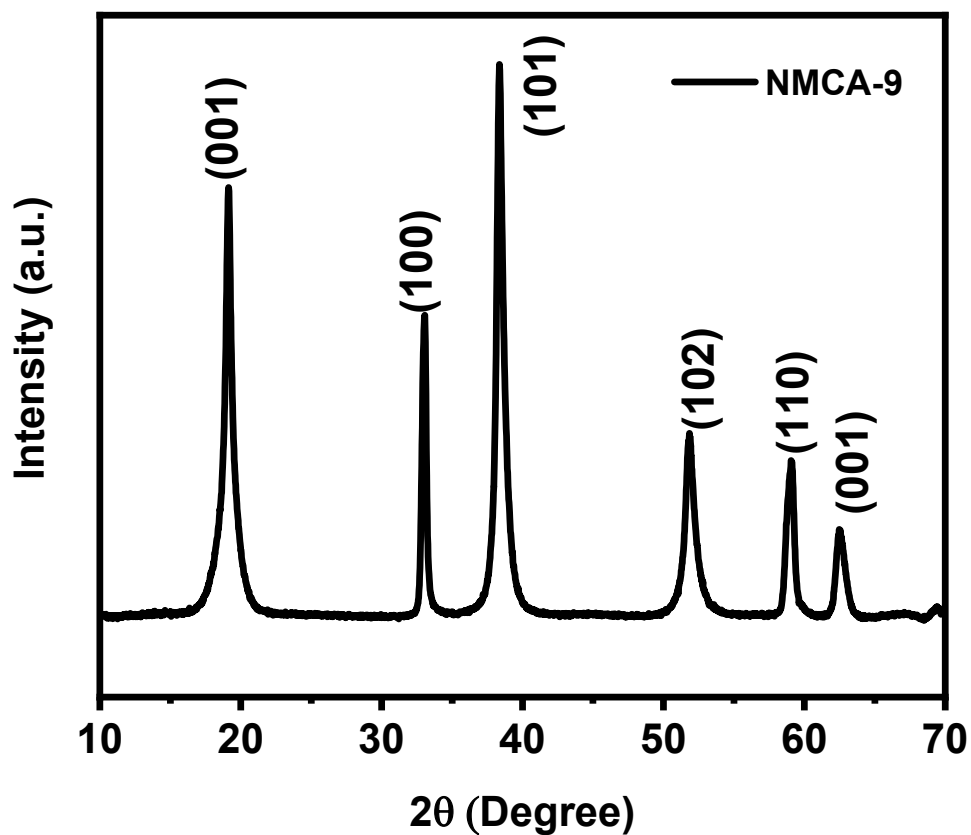


**Fig. S1.** XRD patterns of  $\text{Ni}_{0.90}\text{Mn}_{0.07}\text{Co}_{0.02}\text{Al}_{0.01}(\text{OH})_2$  precursor.

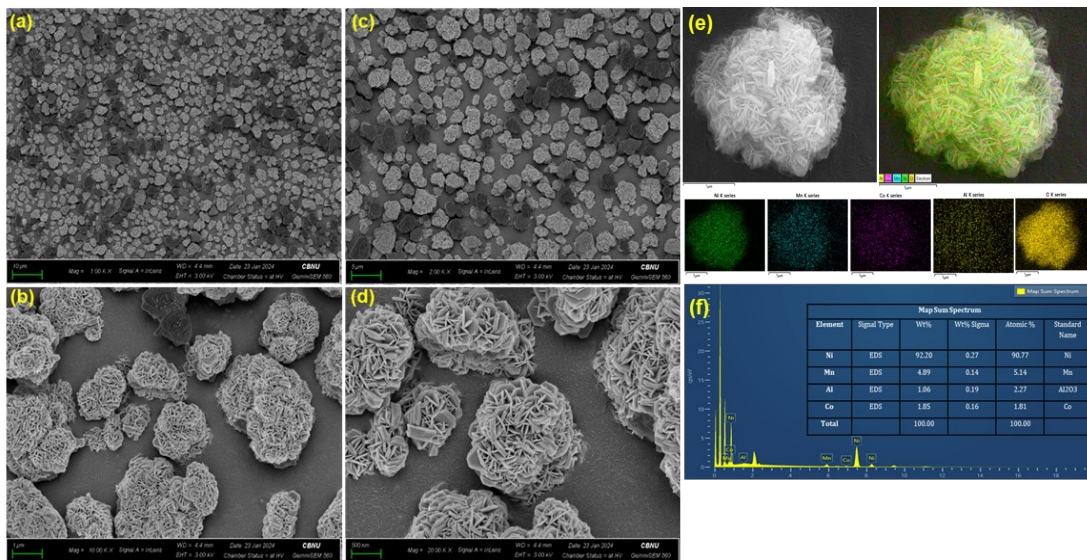


**Fig. S2.** HR-SEM images at different magnifications (a-d), EDX elemental distribution maps (e), and overall spectra (f) of  $\text{Ni}_{0.90}\text{Mn}_{0.07}\text{Co}_{0.02}\text{Al}_{0.01}(\text{OH})_2$  spherical precursor.

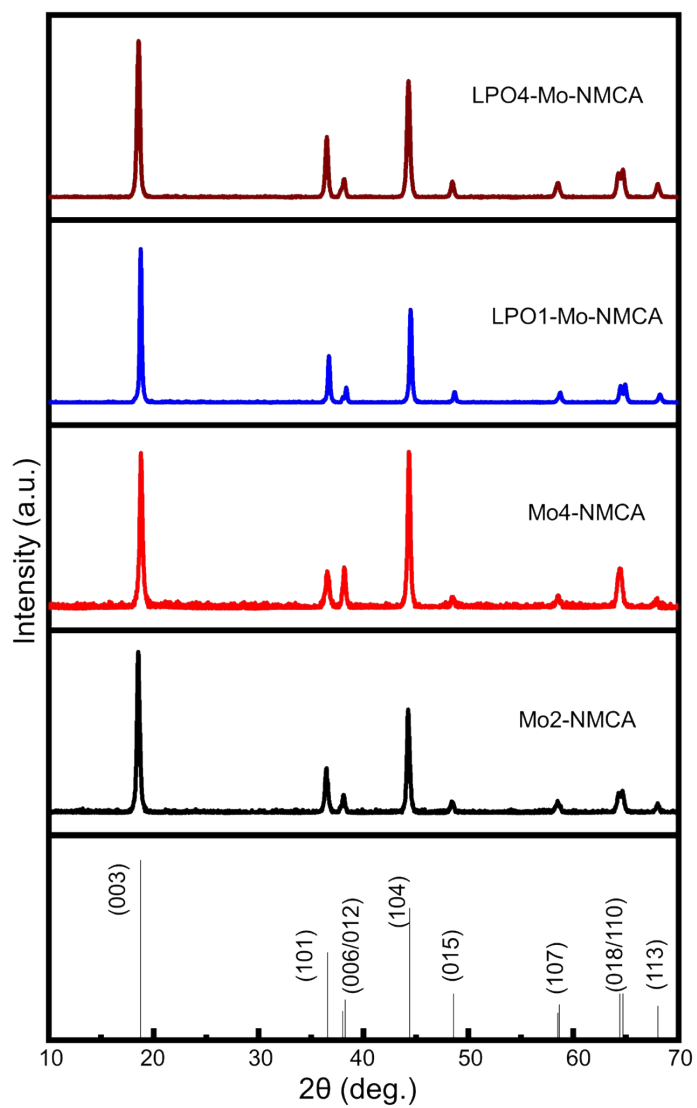


**Fig. S3.** a) Powder XRD patterns of Mo<sub>2</sub>-NMCA, Mo<sub>4</sub>-NMCA, Mo<sub>2</sub>-NMCA, LPO1-NMCA and LPO4-Mo-NMCA samples.

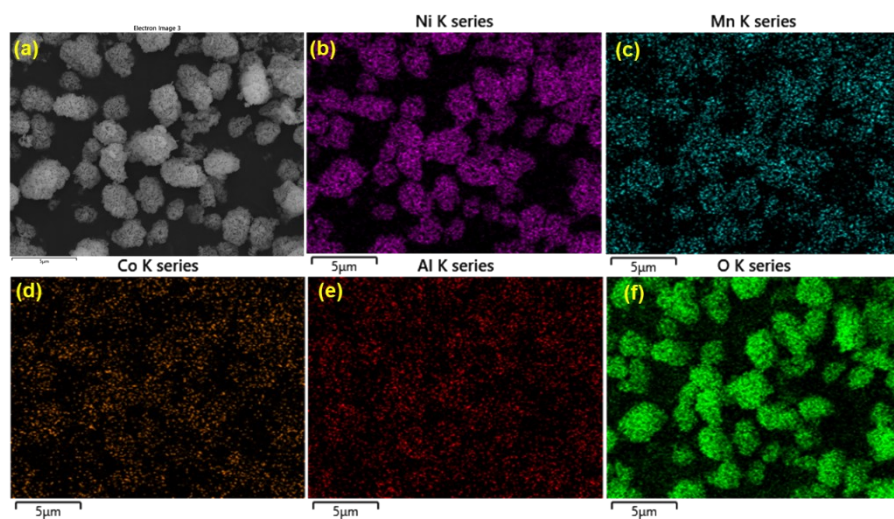


**Fig. S4.** HR-SEM image (a) and corresponding EDX elemental maps (b-f), showing the uniform distributions of Ni, Mn, Co, Al, and O in bare NMCA.

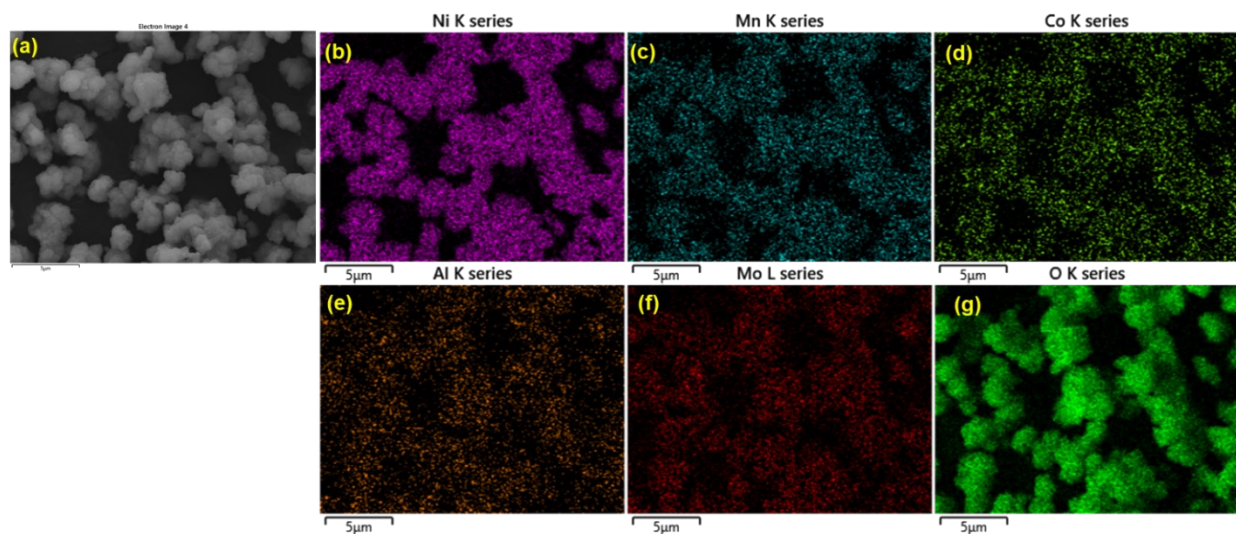


**Fig. S5.** HR-SEM image (a) and corresponding EDX elemental maps (b-g), showing the uniform distributions of Ni, Mn, Co, Al, Mo, and O in Mo-NMCA.



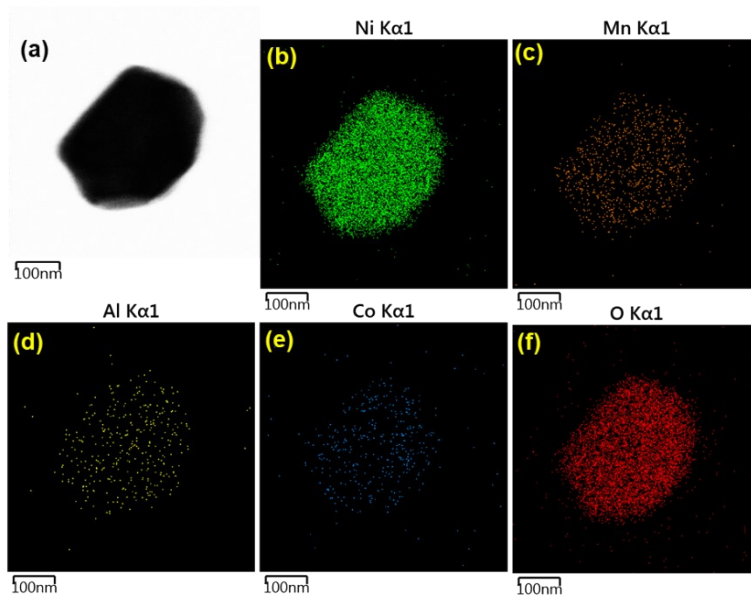


**Fig. S6.** TEM image (a) and corresponding EDX elemental maps (b-f) of the primary particles of NMCA sample, illustrating the uniform distribution of Ni, Mn, Al, Co, and O elements.

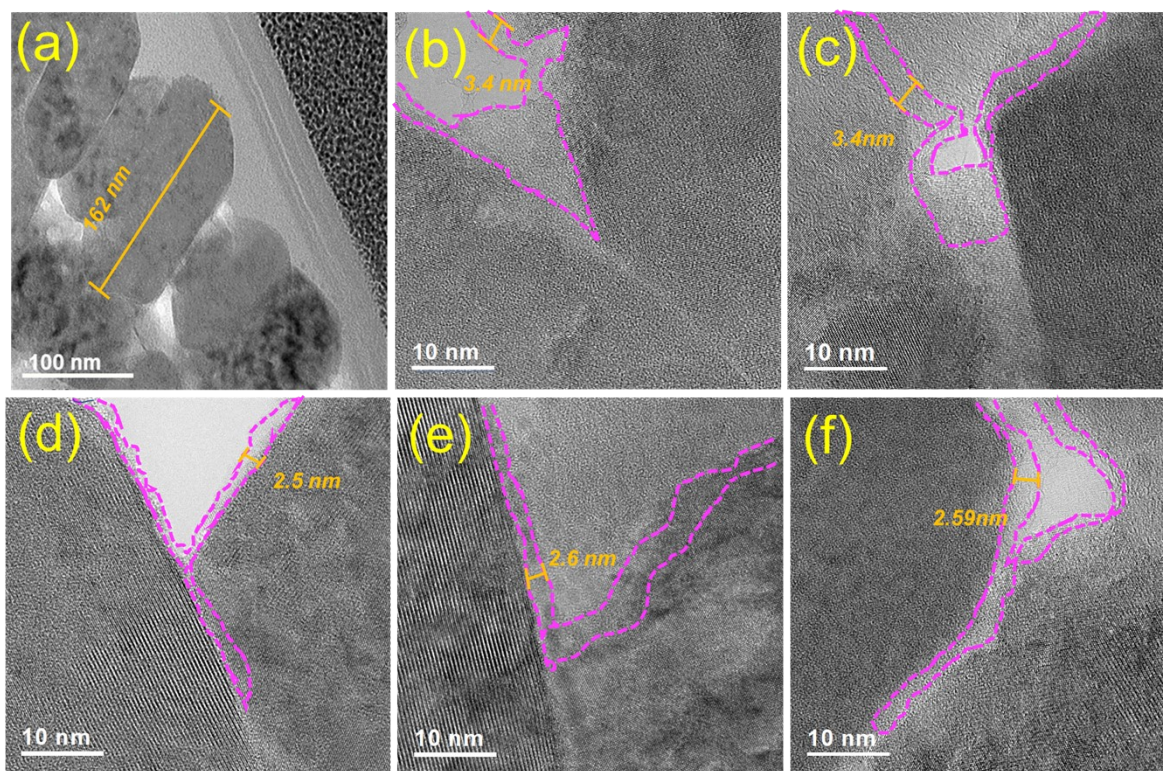


**Fig. S7.** TEM image of LPO–Mo–NMCA primary particle. (b–f) HR-TEM images at various regions confirming the presence of a uniform  $\sim 1.5$  nm LPO surface layer on the Mo–NMCA cathode.

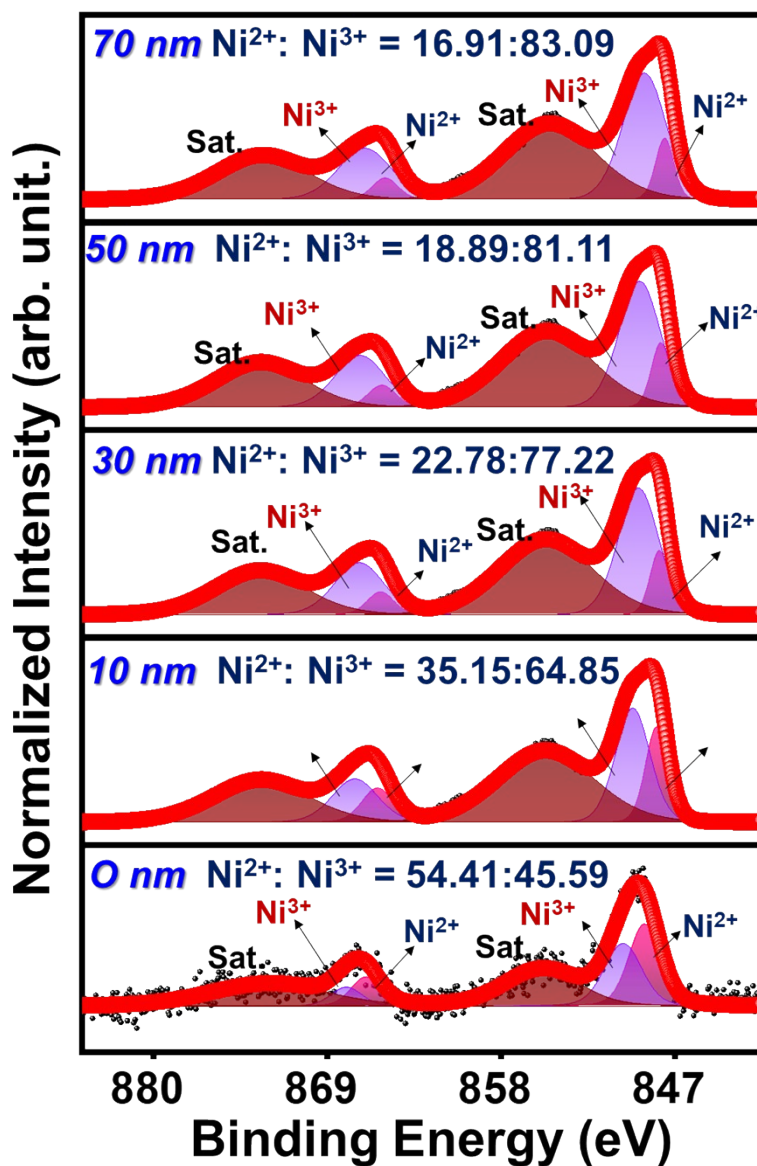


**Fig. S8** XPS spectra of the LPO-Mo-NMCA cathode material showcasing Ar ion sputtering depth profiles at 0, 10, 30, 50, and 70 nm with a focus on the Ni<sup>2+</sup> and Ni<sup>3+</sup> states as revealed by the Ni 2p spectra analysis

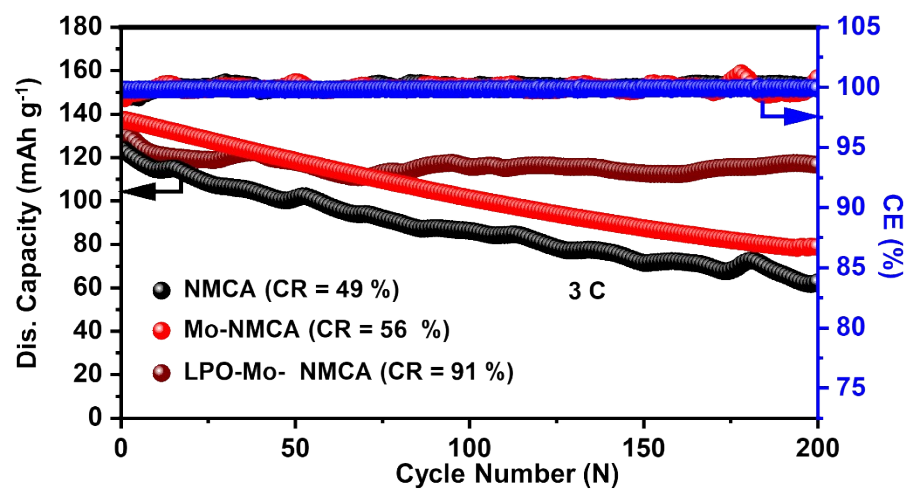


**Fig. S9.** long-term cycling performance of NMCA, Mo-NMCA, and LPO-Mo-NMCA at 3C for 200 cycles.

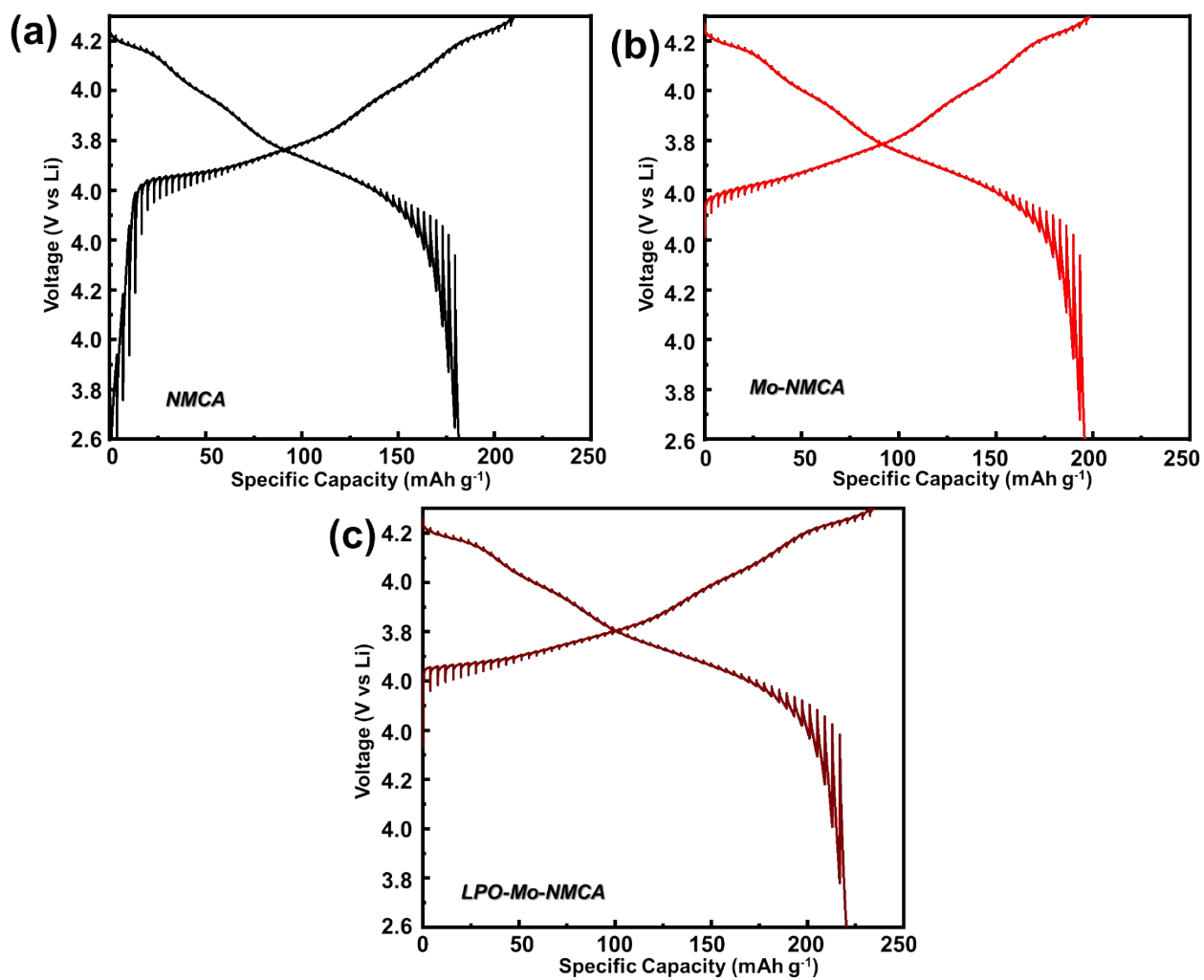


**Fig. S10** GITT curves of (a). NMCA, (b). Mo-NMCA, and (c). LPO2-Mo-NMCA during the first charge/discharge at 0.1 C rate.

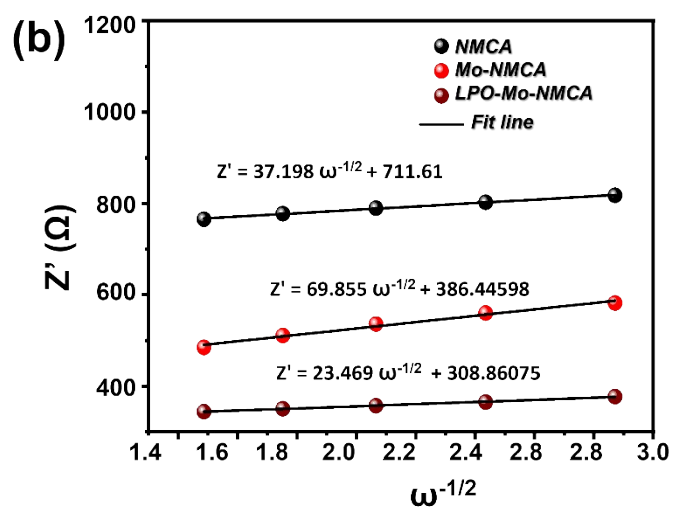
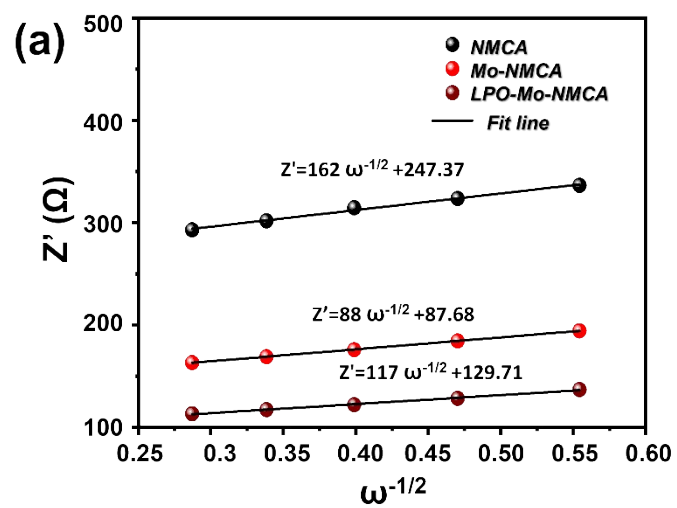
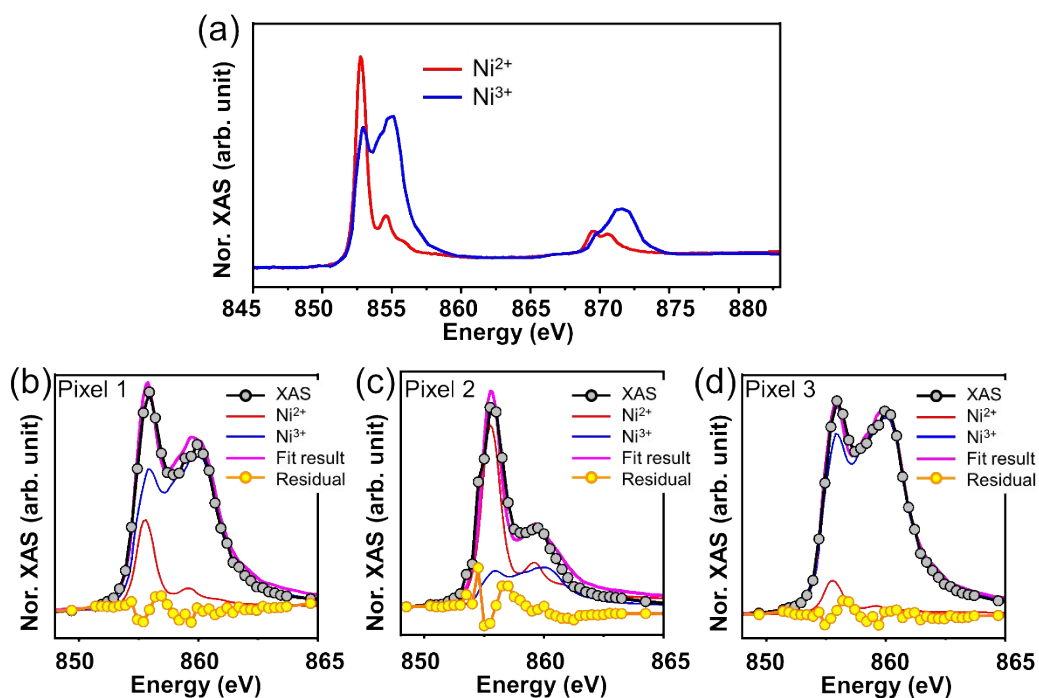
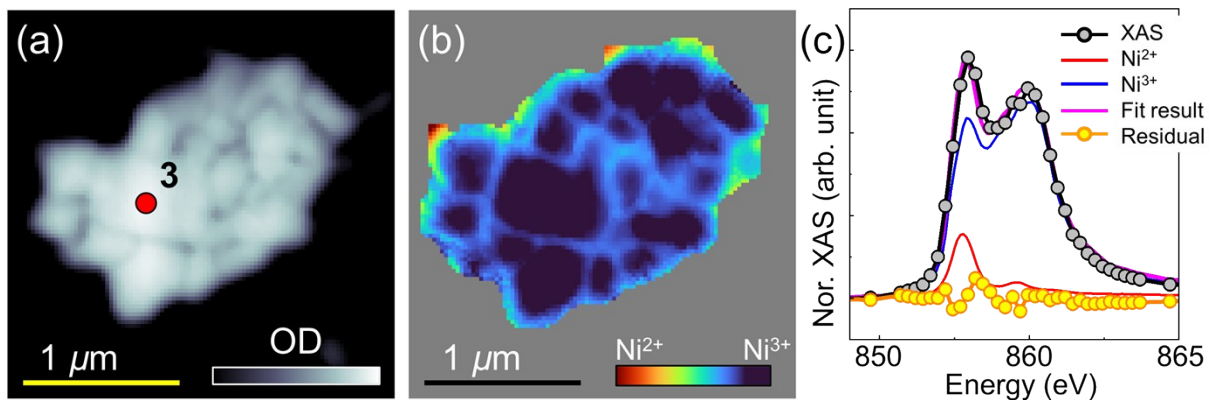


Fig. S11. (a) before and (b) after 200 cycles at 1 C for the typical plots of  $Z'$  vs  $\Omega^{-0.5}$



**Fig. S12.** (a) Reference XAS spectra for Ni<sup>2+</sup> and Ni<sup>3+</sup>, obtained from LiNi<sub>0.8</sub>Co<sub>0.15</sub>Al<sub>0.05</sub>O<sub>2</sub> and LiMn<sub>1.5</sub>Ni<sub>0.5</sub>O<sub>4</sub> spinel, respectively. (b-d) Representative single-pixel-XAS spectra (black lines with scatters) and quantitatively simulated spectra (magenta solid lines) derived from the superposition of the references in (a). The positions of the selected pixels are indicated in Fig 8 and S13. The residues represent the difference between the measured and simulated XAS spectra. The estimated Ni<sup>2+</sup> compositions are 29.8 %, 76.7 %, and 11.0 % for pixels 1-3 in Fig. 8 and S13, respectively.



**Fig. S13.** (a) Microstructure and (b) Ni oxidation state map for a pristine LPO-Mo-NMCA secondary particle obtained using STXM. The oxidation states of Ni ions are presented by a color gradient from red ( $\text{Ni}^{2+}$ ) to blue ( $\text{Ni}^{3+}$ ). (c) Averaged XAS spectrum (black line with scatters) from the entire sample region, along with a quantitatively simulated spectrum (magenta solid line) derived from the superposition of references spectra in Fig. S13(a).

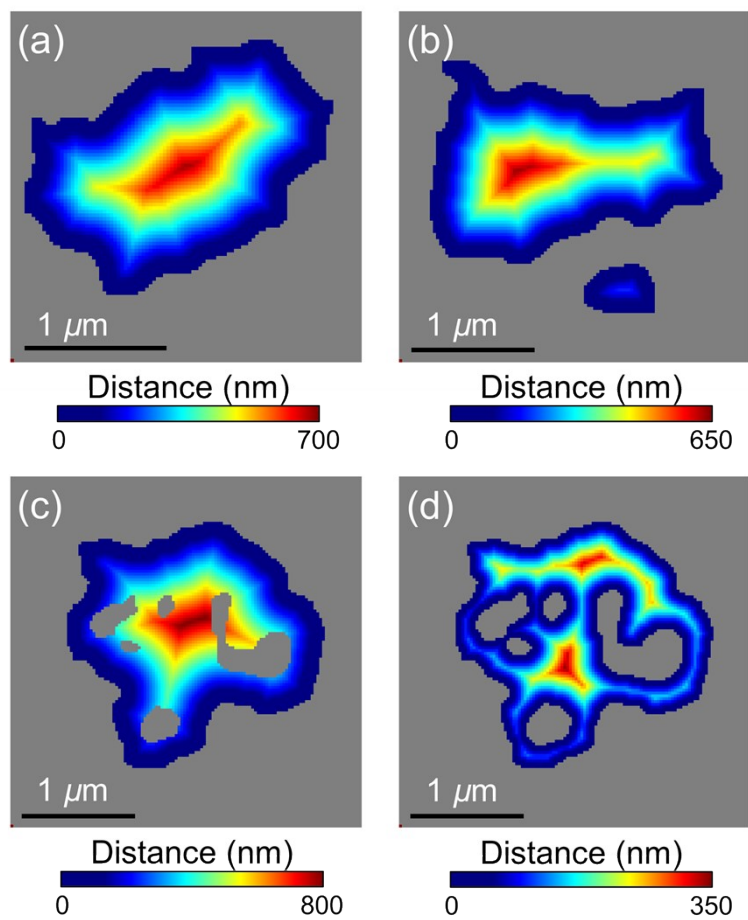


**Fig. S14.** Distance maps from the external surface of the secondary particle for pristine LPO-Mo-NMCA (a and b) and NMCA (c). (d) Distance map from both the internal and external surfaces for pristine NMCA.

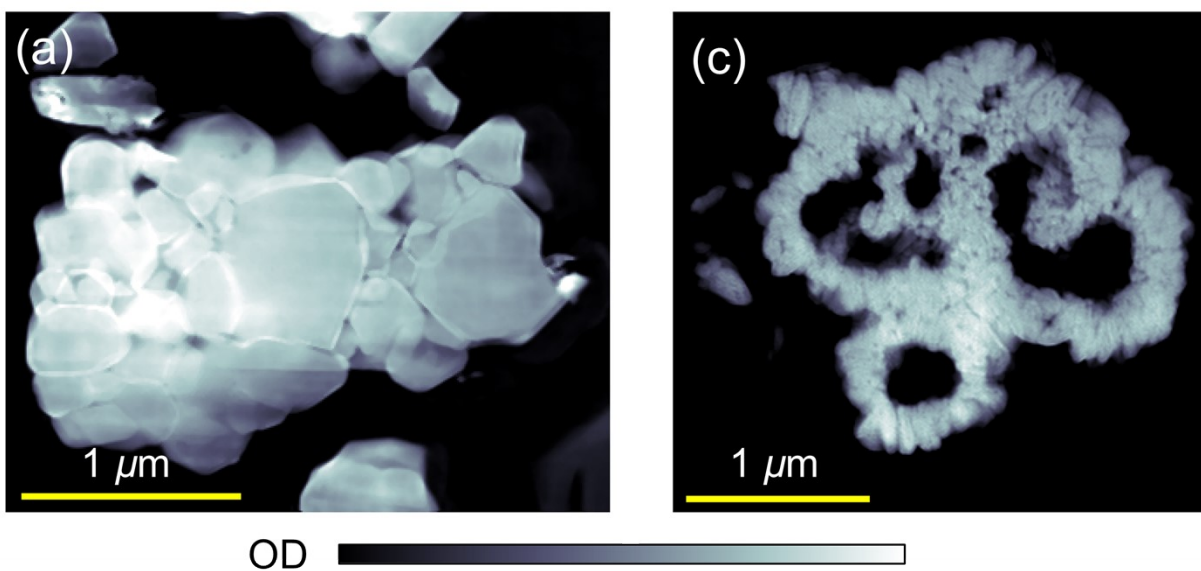


**Fig. S15.** Optical density maps of X-ray-transparent FIB-sliced pristine LPO-Mo-NMCA (a) and NMCA (b) obtained using high-resolution ptychography. The optical density maps were measured at 852.7 eV, where Ni<sup>2+</sup> spectrum has maximum intensity (see the reference spectra in Fig. 12).

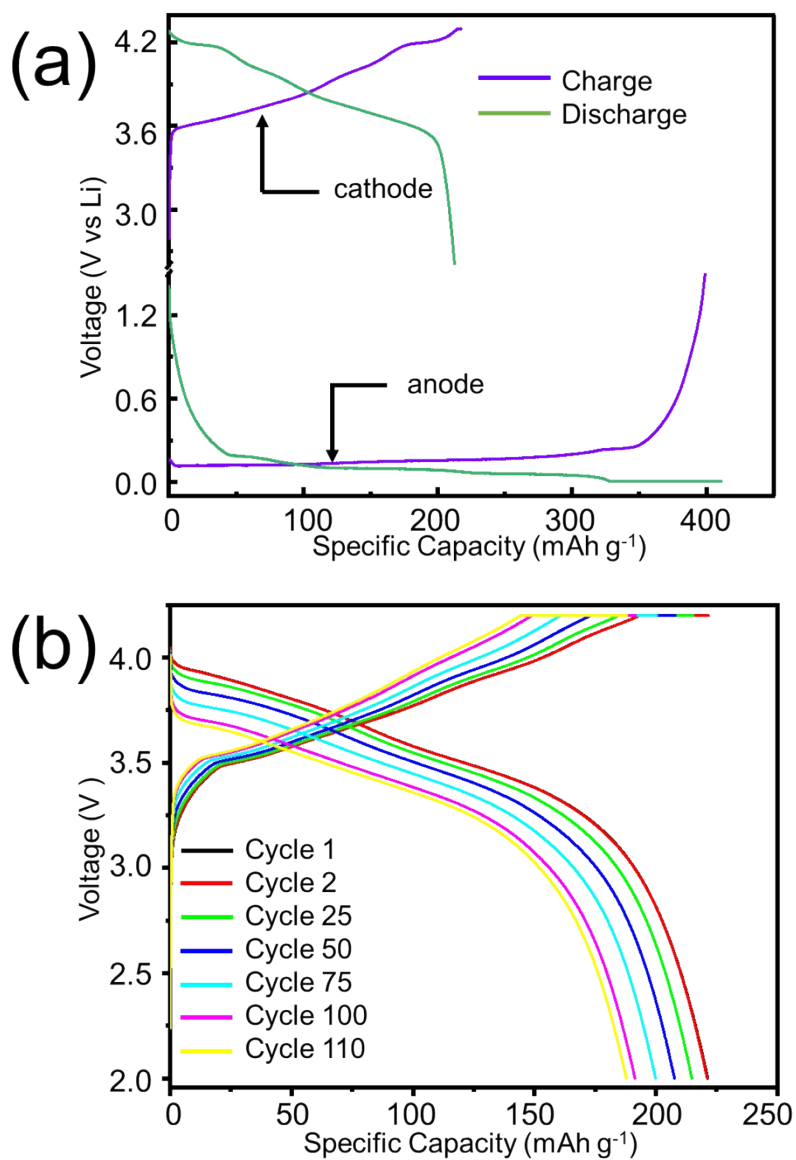


**Fig. S16.** (a) Voltage–capacity curves of the anode and cathode electrodes and (b) charge–discharge profile of the LPO-Mo-NMCA//graphite full cell with an N:P ratio of 1.8:1.

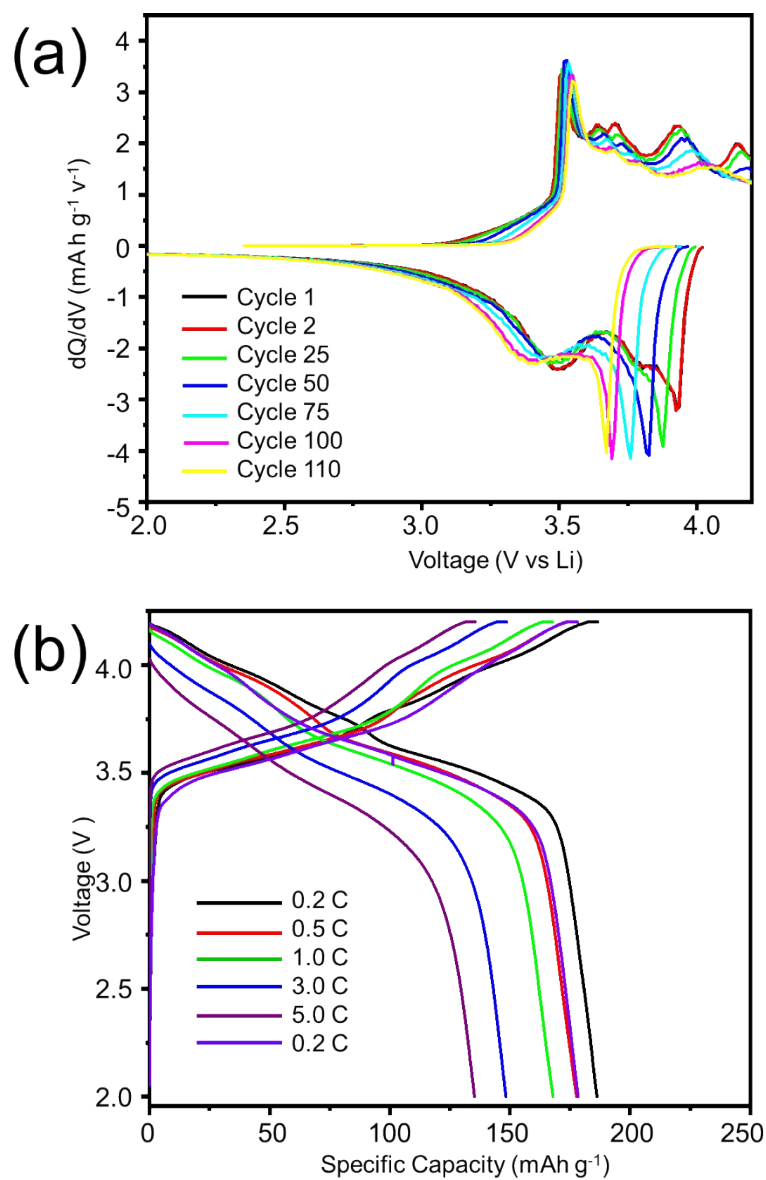


**Fig. S17.** (a) Differential capacity ( $dQ/dV$ ) profile and (b) high C-rate charge/discharge profile of the LPO-Mo-NMCA//graphite full cell with an N:P ratio of 1.8:1.

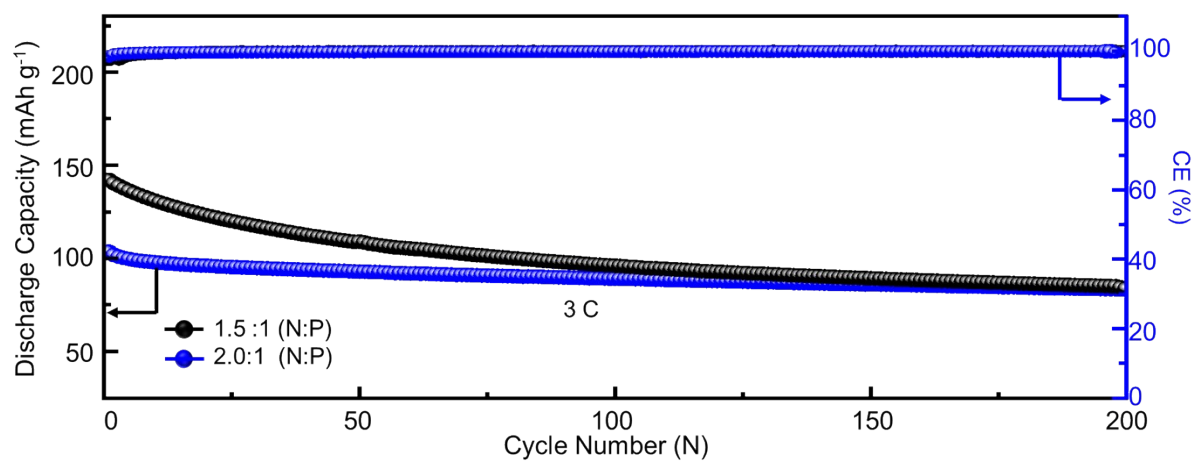


**Fig. S18.** Long-term cycling stability at 3C over 200 cycles for LPO-Mo-NMCA//graphite full cells with optimal N:P ratios of 1.5:1 and 2.0:1.

**Table S1.** Structural parameters of NMCA, Mo-NMCA, and LPO-Mo-NMCA obtained from Rietveld refinement of neutron diffraction patterns.

Parameter	NMCA	Mo-NMCA	LPO-Mo-NMCA
a (Å)	2.87754 (2)	2.88070 (5)	2.87288 (2)
c (Å)	14.1997 (1)	14.2164 (3)	14.1950 (1)
Volume (Å <sup>3</sup> )	101.824 (2)	102.169 (3)	101.462 (2)
R <sub>p</sub> (%)	3.78	4.04	2.85
R <sub>wp</sub> (%)	5.34	5.30	3.83
R <sub>i</sub> (%)	1.86	1.82	1.15
R <sub>F</sub> (%)	1.38	1.33	1.04
Li <sub>2</sub> CO <sub>3</sub> (wt%)	1.2 (1)	4.5 (3)	3.3 (1)
Li <sub>3</sub> PO <sub>4</sub> (wt%)	—	—	2.1 (3)
	NMCA	Mo-NMCA	LPO-Mo-NMCA
Site	<i>x,y,z</i> ; B <sub>iso</sub> ; Occ.	<i>x,y,z</i> ; B <sub>iso</sub> ; Occ.	<i>x,y,z</i> ; B <sub>iso</sub> ; Occ.
Li1	0,0,0; 1.3 (1); 0.962 (2)	0,0,0; 1.8 (4); 0.912 (2)	0,0,0; 1.1 (1); 0.979 (1)
Ni2	0,0,0; 1.3 (1); 0.038 (2)	0,0,0; 1.8 (4); 0.088 (2)	0,0,0; 1.1 (1); 0.021 (1)
Ni1	0,0,0.5; 0.36 (2); 0.835 (2)	0,0,0.5; 0.24 (3); 0.809 (2)	0,0,0.5; 0.13 (2); 0.813 (1)
Co1	0,0,0.5; 0.36 (2); 0.019	0,0,0.5; 0.24 (3); 0.1994	0,0,0.5; 0.13 (2); 0.019
Mn1	0,0,0.5; 0.36 (2); 0.068	0,0,0.5; 0.24 (3); 0.06979	0,0,0.5; 0.13 (2); 0.065
Al1	0,0,0.5; 0.36 (2); 0.010	0,0,0.5; 0.24 (3); 0.00997	0,0,0.5; 0.13 (2); 0.009
Mo1	—	0,0,0.5; 0.24 (3); 0.003	0,0,0.5; 0.13 (2); 0.003
Li2	0,0,0.5; 0.36 (2); 0.068 (2)	0,0,0.5; 0.24 (3); 0.088 (2)	0,0,0.5; 0.13 (2); 0.091 (1)
O1	0,0,0.24177 (7); 1.13 (3); 1.0	0,0,0.2423 (1); 0.82 (4); 1.0	0,0,0.24164 (6); 0.95 (3); 1.0

**Table S2.** Li<sup>+</sup> ion diffusion coefficients of doping/surface-modified cathodes reported in the literature

<b>Cathode Material</b>	<b>Doping/surface modification</b>	<b>D<sub>Li<sup>+</sup></sub> (cm<sup>2</sup> s<sup>-1</sup>)</b>	<b>Method</b>
LiNi <sub>0.5</sub> Co <sub>0.2</sub> Mn <sub>0.3</sub> O <sub>2</sub> <sup>8</sup>	Mo doping	3.8 × 10 <sup>-10</sup>	GITT
LiNi <sub>0.815</sub> Co <sub>0.15</sub> Al <sub>0.05</sub> O <sub>2</sub> <sup>9</sup>	Mn doping	1.6 × 10 <sup>-10</sup>	GITT
LiNi <sub>0.90</sub> Co <sub>0.07</sub> O <sub>2</sub> <sup>10</sup>	Mg gradient	1.61 × 10 <sup>-10</sup>	GITT
LiNi <sub>0.6</sub> Co <sub>0.2</sub> Mn <sub>0.2</sub> O <sub>2</sub> <sup>11</sup>	BO <sub>3</sub> <sup>3-</sup>	ca. 10 <sup>-8</sup>	GITT
LiNi <sub>0.8</sub> Co <sub>0.1</sub> Mn <sub>0.1</sub> O <sub>2</sub> <sup>12</sup>	Li <sub>5</sub> AlO <sub>4</sub>	5.37 × 10 <sup>-11</sup>	GITT
LiNi <sub>0.90</sub> Co <sub>0.04</sub> Mn <sub>0.03</sub> Al <sub>0.03</sub> O <sub>2</sub> <sup>13</sup>	Li <sub>2</sub> ZrO <sub>3</sub>	5.37 × 10 <sup>-10</sup>	GITT
<b>LPO-Mo-NMCA (This work)</b>	<b>Mo doping and LPO</b>	<b>Ca. ×10<sup>-9</sup> to x 10<sup>-10</sup></b>	<b>GITT</b>

**Table S3.** Resistance and D<sub>Li<sup>+</sup></sub> obtained from the simulation with the equivalent circuits

<b>Samples Name</b>	<b>Before Cycle</b>			<b>After 200<sup>th</sup> cycle</b>			
	<b>R<sub>s</sub> (Ω)</b>	<b>R<sub>ct</sub> (Ω)</b>	<b>D<sub>Li<sup>+</sup></sub> (cm<sup>2</sup>·s<sup>-1</sup>)</b>	<b>R<sub>s</sub> (Ω)</b>	<b>R<sub>SEI</sub> (Ω)</b>	<b>R<sub>ct</sub> (Ω)</b>	<b>D<sub>Li<sup>+</sup></sub> (cm<sup>2</sup>·s<sup>-1</sup>)</b>
<b>NMCA</b>	2.54	248.54	8.17x 10 <sup>-12</sup>	6.84	242.06	648.52	4.29 x 10 <sup>-13</sup>
<b>Mo-NMCA</b>	3.32	141.54	2.32 x 10 <sup>-12</sup>	4.47	209.66	561.54	8.32x 10 <sup>-13</sup>
<b>LPO-Mo-NMCA</b>	3.33	89.85	2.05 x 10 <sup>-11</sup>	4.24	168.81	235.32	1.46x 10 <sup>-12</sup>

**Table S4.** Comparison of specific capacity and energy density of recently reported Ni-rich cathode materials in full-cell lithium-ion batteries.

Cathode	Anode	Voltage range (V)	Working voltage (V)	Specific capacity (mAh/g)	Energy Density (Wh/kg)
$\text{LiNi}_{1/3}\text{Mn}_{1/3}\text{Co}_{1/3}\text{O}_2$ <sup>14</sup>	Graphene/Si	3.0–4.3	3.7	137 at C/15	156 and at 23 mA g <sup>-1</sup>
$\text{LiNi}_x\text{Co}_y\text{Mn}_{1-x-y}\text{O}_2$ <sup>15</sup>	$\text{Li}_{4/3}\text{Ti}_{5/3}\text{O}_4$	1.5–2.7	2.3		90 at 1 A/g
$\text{LiNi}_{0.75}\text{Co}_{0.1}\text{Mn}_{0.15}\text{O}_2$ <sup>16</sup>	Si/CIWGS	2.7–4.2	3.6	196 at 0.1	720 at 200 mA/g
Nb doped $\text{LiNi}_{0.9}\text{Co}_{0.1}\text{O}_2$ <sup>17</sup>	meso-microbeads carbon	3.0-4.2	3.5	229 at 0.1	-
$\text{LiNi}_{0.85}\text{Co}_{0.12}\text{Al}_{0.03}\text{O}_2$ <sup>18</sup>	Graphite	2.8-4.3			-
$\text{LiNi}_{0.94}\text{Co}_{0.05}\text{Te}_{0.01}\text{O}_2$ <sup>19</sup>	silicon	2.7-4.6	3.8	239 at 0.1 C	404 at 0.5 C
$\text{Li}[\text{Ni}_{0.885}\text{Co}_{0.100}\text{Al}_{0.015}]_{20}\text{O}_2$	Graphite	3.0-4.2	-	195 at 1 C	-
$\text{LiNi}_{0.6}\text{Mn}_{0.2}\text{Co}_{0.2}\text{O}_2$ <sup>21</sup>	$\text{Li}_4\text{Ti}_5\text{O}_{12}$	1.6 – 2.65	-	85 at 1 C	-
LPO-Mo-NMCA (This work)	Graphite	2 – 4.2	3.6	218 at 0.1 C	362.2 at 0.1 C

## References

1. D. A. Shapiro, S. Babin, R. S. Celestre, W. Chao, R. P. Conley, P. Denes, B. Enders, P. Enfedaque, S. James and J. M. Joseph, *Science advances*, 2020, **6**, eabc4904.
2. H. J. Shin, N. Kim, H. S. Kim, W. W. Lee, C. S. Lee and B. Kim, *Journal of Synchrotron Radiation*, 2018, **25**, 878-884.
3. D. Ziegler, T. R. Meyer, A. Amrein, A. L. Bertozzi and P. D. Ashby, *IEEE/ASME Transactions on Mechatronics*, 2016, **22**, 381-391.
4. D. A. Shapiro, Y.-S. Yu, T. Tyliczszak, J. Cabana, R. Celestre, W. Chao, K. Kaznatcheev, A. L. D. Kilcoyne, F. Maia and S. Marchesini, *Nature Photonics*, 2014, **8**, 765-769.
5. Y.-S. Yu, M. Farmand, C. Kim, Y. Liu, C. P. Grey, F. C. Strobridge, T. Tyliczszak, R. Celestre, P. Denes and J. Joseph, *Nature Communications*, 2018, **9**, 921.
6. N. Otsu, *Automatica*, 1975, **11**, 23-27.
7. D. Y. Hwang, C. Y. Kang, J. R. Yoon and S. H. Lee, *International Journal of Energy Research*, 2022, **46**, 15244-15253.
8. Y. Zhang, Z.-B. Wang, F.-D. Yu, L.-F. Que, M.-J. Wang, Y.-F. Xia, Y. Xue and J. Wu, *Journal of Power Sources*, 2017, **358**, 1-12.
9. C.-L. Xu, W. Xiang, Z.-G. Wu, Y.-D. Xu, Y.-C. Li, M.-Z. Chen, G. XiaoDong, G.-P. Lv, J. Zhang and B.-H. Zhong, *ACS Applied Materials & Interfaces*, 2018, **10**, 27821-27830.
10. Y. Zhang, H. Li, J. Liu, J. Zhang, F. Cheng and J. Chen, *Journal of Materials Chemistry A*, 2019, **7**, 20958-20964.
11. Y. Zhang, T. Ren, J. Zhang, J. Duan, X. Li, Z. Zhou, P. Dong and D. Wang, *Journal of Alloys and Compounds*, 2019, **805**, 1288-1296.
12. J. Zhou, Q. Wang, M. Zhang, Y. Guo, A. Zhu, X. Qiu, H. Wu, X. Chen and Y. Zhang, *Electrochimica Acta*, 2020, **353**, 136541.
13. J. Jeyakumar, Y.-S. Wu, S.-H. Wu, R. Jose and C.-C. Yang, *ACS Applied Energy Materials*, 2022, **5**, 4796-4807.
14. L. Ji, H. Zheng, A. Ismach, Z. Tan, S. Xun, E. Lin, V. Battaglia, V. Srinivasan and Y. Zhang, *Nano Energy*, 2012, **1**, 164-171.
15. N. Takami, H. Inagaki, Y. Tatebayashi, H. Saruwatari, K. Honda and S. Egusa, *Journal of power sources*, 2013, **244**, 469-475.
16. C. Chae, H. J. Noh, J. K. Lee, B. Scrosati and Y. K. Sun, *Advanced Functional Materials*, 2014, **24**, 3036-3042.
17. H. Zhu, Z. Wang, L. Chen, Y. Hu, H. Jiang and C. Li, *Advanced Materials*, 2023, **35**, 2209357.
18. M. Kim, W. Lee, E. Lee, J. Kim, J. U. Kim, S. Lee, S. Hwang, D. Park, K. Cho and W. S. Yoon, *Advanced Energy Materials*, 2023, **13**, 2302209.
19. T. Yang, K. Zhang, Y. Zuo, J. Song, Y. Yang, C. Gao, T. Chen, H. Wang, W. Xiao and Z. Jiang, *Nature Sustainability*, 2024, **7**, 1204-1214.
20. U.-H. Kim, L.-Y. Kuo, P. Kaghazchi, C. S. Yoon and Y.-K. Sun, *ACS energy letters*, 2019, **4**, 576-582.
21. I. A. Moiseev, A. A. Savina, A. D. Pavlova, T. A. Abakumova, V. S. Gorshkov, E. M. Pazhetnov and A. M. Abakumov, *Energy Advances*, 2022, **1**, 677-681.